Anti-symmetric sampled grating quantum cascade laser for mode selection

Qiangqiang Guo(郭强强)[1,2], Jinchuan Zhang(张锦川)[1,†], Fengmin Cheng(程凤敏)[1,2], Ning Zhuo(卓宁)[1], Shenqiang Zhai(翟慎强)[1], Junqi Liu(刘俊岐)[1,2], Lijun Wang(王利军)[1,2], Shuman Liu(刘舒曼)[1,2], and Fengqi Liu(刘峰奇)[1,2,‡]

[1] *Key Laboratory of Semiconductor Materials Science, Institute of Semiconductors, Chinese Academy of Sciences, Beijing Key Laboratory of Low Dimensional Semiconductor Materials and Devices, Beijing* 100083, *China*

[2] *Center of Materials Science and Optoelectronics Engineering, University of Chinese Academy of Sciences, Beijing* 100049, *China*

(Received 26 February 2022; revised manuscript received 10 May 2022; accepted manuscript online 24 May 2022)

For mode selection in a quantum cascade laser (QCL), we demonstrate an anti-symmetric sampled grating (ASG). The wavelength of the −1-th mode of this laser has been blue-shifted more than 75 nm (~ 10 cm^{-1}) compared with that of an ordinary sampled grating laser with an emission wavelength of approximately 8.6 μm, when the periodicities within both the base grating and the sample grating are kept constant. Under this condition, an improvement in the continuous tuning capability of the QCL array is ensured. The ASG structure is fabricated in holographic exposure and optical photolithography, thereby enhancing its flexibility, repeatability, and cost-effectiveness. The wavelength modulation capability of the two channels of the grating is insensitive to the variations in channel size, assuming that the overall waveguide width remains constant. The output wavelength can be tailored freely within a certain range by adjusting the width of the ridge and the material of the cladding layer.

Keywords: sample grating, tilted grating, quantum cascade laser, mode selection

PACS: 42.79.Dj, 42.55.Px, 42.60.Fc **DOI:** 10.1088/1674-1056/ac7291

1. Introduction

The quantum cascade laser (QCL) is a unipolar semiconductor laser that operates via the intersubband transitions in the conduction band.[1–5] Since it was firstly demonstrated in 1994, the QCL has attracted a lot of attention in basic and applied research. Steady developments have widened its operating frequency to cover the mid-infrared to the terahertz regions. It is currently the most ideal semiconductor laser source for the mid-/far-infrared frequency region. Stable single-mode emission and wide-range tunability over a certain wavelength range are of great importance in sensing and spectroscopy applications.[6–9] Data acquisition of multiple wavelengths improves the accuracy in detection enabling substances (especially biological macromolecules) with similar spectral fingerprints to be distinguished.[10–13] However, practical applications for single distributed-feedback (DFB) QCLs are strongly limited because their tuning range is less than 10 cm^{-1}.

There are three main types of tunable QCLs available for spectroscopy and sensing applications: the external-cavity (EC) QCL, the dual-section sampled grating QCL, and the DFB-QCL array. Whereas the tuning range of the EC-QCL covers the entire gain area, the free tuning of each mode is limited by its mechanical tuning system.[14,15] The tuning behavior of the dual-section sampled grating QCL by using the Vernier effect is usually inconsistent with theoretical predictions because of mode competition and spatial hole burning.[16,17] The tuning range of the DFB-QCL array, which is composed of a number of lasers, can also be extended to hundreds of wavenumbers because every array element emits at a distinct wavelength selected by the grating periodicity. Usually fabricated with high-cost electron beam lithography,[18] the sampled grating is an effective means of reducing costs in array fabrication. The realization of wavelength tuning relies only on the micron-level sampling pattern imprinted on a uniform base grating. For the fabrication of the sampled grating, only holographic exposure and optical photolithography are required.[19–21]

The 0-th order mode of the sampled grating is not modulated by the sampled grating, and usually the −1-th or +1-th order mode is selected as the emission mode. The periodicity of the sampled grating varies from element to element and hence the array emits different wavelengths spanning a desired region. Ideally, the wavelength spacing between the adjacent emission modes should be less than the feasible range for temperature tuning. To extend the tuning range further, the grating periodicity must be short enough. Challenges arise in producing a precise grating periodicity because the wavelength spacing between adjacent emission modes increases sharply with shorter periodicities. In consequence, a discontinuous tuning of wavelengths occurs despite the tuning range of the temperature being close to 10 cm^{-1}. Therefore, a more advanced

†Corresponding author. E-mail: zhangjinchuan@semi.ac.cn
‡Corresponding author. E-mail: fqliu@semi.ac.cn

© 2023 Chinese Physical Society and IOP Publishing Ltd

tuning mechanism is needed to optimize the tuning capability of the sampled grating. In the field of optical communications, changing the wavelength spacing between the 0-th and the −1-th order modes by using an anti-symmetric sampled grating (ASG) structure has been theoretically confirmed. Nevertheless, the periodicity of both the base and sample gratings are assumed to be kept constant.[22]

In this work, we designed and manufactured an ASG QCL for which a stable single-mode emission was achieved. Under continuous wave operations at room temperature, the wavelengths of the emission were approximately 8.6 μm. Among them, the wavelength of the −1-th order mode was blue-shifted by more than 75 nm (∼ 10 cm^{-1}), and the current tuning coefficient is nevertheless consistent with that of ordinary sampled grating devices. We demonstrated that the simulation results using the finite-element method (FEM) are in good agreement with those from experimental tests. Moreover, the structure of the ASG is highly robust against size fluctuations in the two channels of the grating, assuming that the overall waveguide width remains constant. The output wavelength can be tailored freely within a certain range by adjusting the widths of the ridge and the cladding material. Such flexibility is very advantageous in the manufacturing of QCL arrays with sampled gratings and their practical application.

2. Device design

The basic principle of the ordinary sampled grating rests on the formulas

$$\lambda_0 = 2n_{\text{eff}}\Lambda_0, \tag{1}$$

$$\frac{1}{\lambda_{-2}} - \frac{1}{\lambda_{-1}} = \frac{1}{\lambda_{-1}} - \frac{1}{\lambda_0} = \frac{1}{2n_{\text{eff}}Z}, \tag{2}$$

where λ_0 denotes the wavelength of the base grating, Λ_0 and Z denote the periodicities of the base and sample gratings, respectively, λ_{-1} and λ_{-2} the wavelengths of the modes of order -1 and -2, and n_{eff} denotes the effective refractive index of the whole waveguide (the cladding on both sides of the ridge makes no contribution to the ordinary sampled grating).

Figure 1 shows the electroluminescence spectrum (lower curve) of the epitaxial wafer, recorded at room temperature by using a Fourier transform infrared spectrometer with a pulse width of 2 μs and a repetition frequency of 30 kHz. The peak of the gain curve is about 8.42 μm and the full width at half-maximum is about 160 cm^{-1}. The value of n_{eff} measured for the entire waveguide is 3.187 (assuming the holographic exposure period is accurate and reliable, and the grating duty cycle is 50%). Here we set the base grating periodicity to 1.59 μm, corresponding to a wavelength of 10.135 μm (upper curve). This value is far from the center of the gain spectrum so that a sufficient gain cannot be obtained and is suppressed. Hence, the sampled grating periodicity is set to be 10 μm, corresponding to the −1-th order mode wavelength of 8.744 μm. To ensure the stable single-mode emission and to suppress the band-edge mode, the defect mode (Fig. 1 inset; the defect mode is emitted firstly before the band-edge mode) is introduced through a quarter-wave equivalent phase shift (EPS).

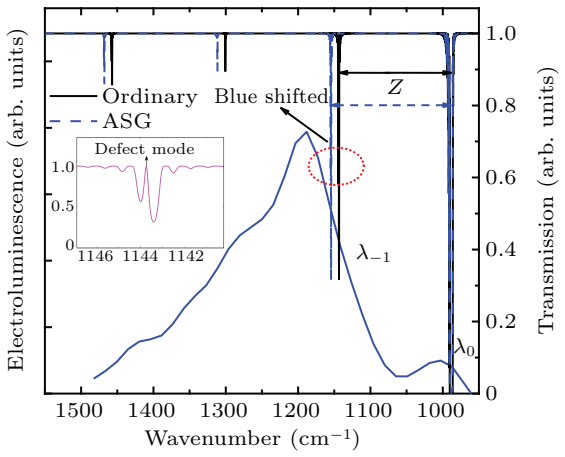


Fig. 1. Electroluminescence spectrum and the calculated transmission spectrum. The −1-th order mode of the ordinary sampled grating is located near the peak in gain, whereas the 0-th order mode is far from the gain range. The inset shows the details of the −1-th order mode with a quarter-wave EPS.

Figure 2(a) shows the structure of the ASG with the quarter-wave equivalent phase shift (EPS). This structure includes two adjacent uniformly sampled gratings with the same periodicity, and they share the same uniform base grating (both are consistent with the ordinary sampled grating). In comparison, there is an additional π phase shift between the two channels at the initial position that produces a modulation of the −1-th order mode of the ASG (the base wavelength is not modulated by the sampled grating). Light propagation in the ASG occurs through total internal reflections (Fig. 2(b)); as the light propagates axially along the waveguide, it also bounces back and forth transversely in the ASG. Therefore, the ASG is equivalent to a two-dimensional lattice structure periodically extending in the transverse direction of the waveguide. With this geometric equivalence, and applying a Fourier analysis, two symmetrical grating wave vectors for the lattice K_{g1} and K_{g2} dominate (Fig. 2(c)). This circumstance is normally associated with a symmetrical two-dimensional tilted grating with tilt angles of $\alpha = \arctan(\Lambda_{\pm}/2w + 4d)$, where $\Lambda_{\pm} = \Lambda_0 Z/(\Lambda_0 \pm Z)$, w the width of the ridge, and d the penetration depth of light in the cladding layer given by $d = 1/[k_0(n_{\text{eff}}^2 - n_{\text{clad}}^2)^{1/2}]$. The wavelength associated with this tilted grating is given as

$$\lambda_{\text{B}} = 2nd_0 \sin\theta, \tag{3}$$

where $n = n_{\text{core}}$, θ denotes the glancing angle given by $\theta = \beta - \alpha$, $\beta = \arcsin(n_{\text{eff}}/n_{\text{core}})$, and d_0 the periodicity of the tilted grating, with $d_0 = \Lambda_{\pm}\cos\alpha$. Substitutions help re-express

the wavelength as

$$\lambda_{\mathrm{B}} = 2n_{\mathrm{core}}\Lambda_{\pm}\cos(\alpha)\sin(\beta-\alpha), \tag{4}$$

Therefore, the wavelength of the equivalent tilted grating is smaller than that for the −1-th order mode of the ordinary sampled grating, whereas both gratings retain the same base wavelength. In general, the −1-th wavelength of the ASG has a wavelength that is blue-shifted compared with that of the ordinary sampled grating (Fig. 1), with the shift being

$$\Delta\lambda_{-1} = 2n_{\mathrm{core}}\frac{\Lambda_0 Z}{\Lambda_0 - Z}[\sin\beta - \cos\alpha\sin(\beta-\alpha)]. \tag{5}$$

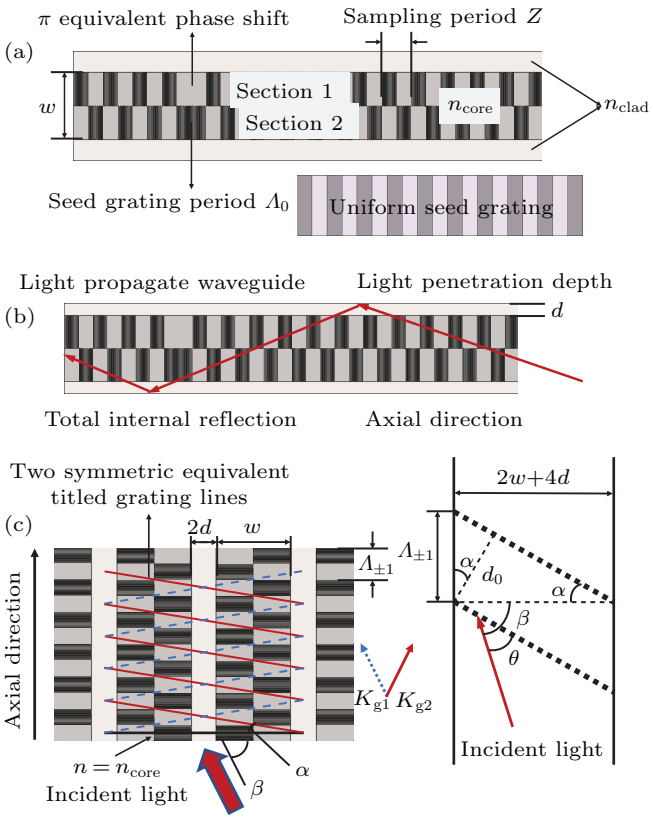


Fig. 2. Schematics associated with the operation of the ASG: (a) grating structure with a quarter-wave equivalent phase shift, (b) total internal reflection of light propagating through the grating — while propagating axial-wise through the waveguide, light bounces back and forth transversely through the ASG, (c) equivalent two-dimensional lattice structure, and (d) geometric diagram of an equivalent tilted grating used in calculating the wavelength.

3. Finite element modeling

To assist in describing the modulation of the −1-th order mode wavelength of the ASG, the electric field distributions (normE) corresponding to the eigenmode spectra of the ordinary sampled grating and the ASG were computed by using an FEM solver (Fig. 3(a)). The lasing frequency is estimated from an analysis of the eigenfrequencies and the electric field distributions. Employing the mechanism describing the refractive index modulation of an ordinary sampled grating and an ASG, two-dimensional simulations are effective in solving the above problems. The two simulation structures have the same uniform base periodicity Λ_0 of 1.59 μm and sampled grating periodicity Z of 10 μm, taking $n_{\mathrm{core}} = 3.187$ and $n_{\mathrm{clad}} = 3.099$. As we have seen, the electric field intensity for the −1-th order mode of the ordinary sampled grating is mostly confined to the grating area and propagates along the axis direction. In comparison, the electric field intensity of the same mode for the ASG bounces periodically in the transverse direction while propagating along the axial direction of the waveguide. Obviously, the wavelength of the −1-th order mode is modulated by the ASG and the cladding on both sides of the ridge and perfectly matches the total internal reflection model described above (Fig. 2).

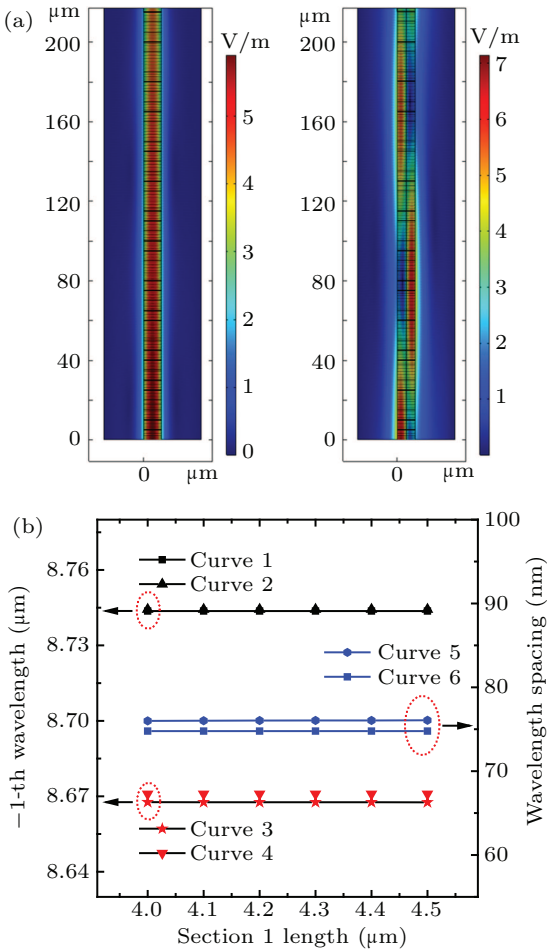


Fig. 3. Finite-element simulation results for the ordinary-sampled grating and ASG, with InGaAs as the high-index material (3.19), InP as the low-index material (3.184), the Fe-doped InP as cladding material (3.099), and the width of the ridge set at 9 μm: (a) Comparison of the electric field distributions of the resonant mode between the ordinary sampled grating (left) and ASG (right). The electric field intensity for the −1-th order mode of the ordinary sampled grating is mostly limited to the grating area. The electric field intensity for −1-th order mode of the ASG propagates along the axial direction and periodically bounces transversely within the waveguide. (b) The variation in the wavelength of the −1-th order mode corresponding to the ASG, with the width of channel 1 varying from 4 μm to 4.5 μm in steps of 0.1 μm; the width of the waveguide remains constant. For the −1-th order mode, curves 1 and 2 indicate its wavelength obtained from FEM simulation of the ordinary sampled grating and formula (2), respectively. Similarly, curves 3 and 4 indicate the wavelength obtained from FEM simulations of the ASG and formula (4), respectively. Curves 5 and 6 respectively indicate the blue-shifted wavelengths obtained from FEM of the ASG and formula (5), respectively.

Under our laboratory conditions, guaranteeing a perfect symmetrical layout of the two channels of the ASG is difficult. In response to this situation, we simulated and analyzed the process tolerance of this structure. The variation in the wavelength of the −1-th order mode for ordinary-sampled grating and ASG (Fig. 3(b)), with channel 1 widths varying from 4.0 μm to 4.5 μm in steps of 0.1 μm, was investigated with the overall waveguide width remaining constant.

Curves 1 and 2 present the results for the ordinary sampled gratings obtained from FEM simulations and Eq. (2), respectively. Similarly, curves 3 and 4 present those for the ASGs obtained from FEM simulations and Eq. (4), respectively, and curves 5 and 6, the blue-shifted wavelengths of the ASGs obtained from FEM simulations and Eq. (5), respectively. A very small fluctuation (a few hundredths of nanometers) is evident in the simulation result with the size of channel 1, sufficient to show that this structure is very robust.

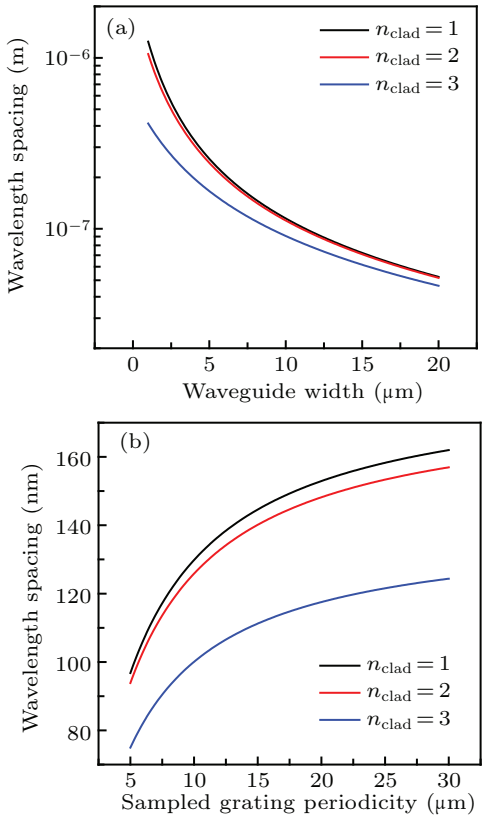


Fig. 4. Calculated results for the ASGs with different structural parameters. (a) The blue-shifted wavelengths as a function of waveguide width for different cladding materials, with the same sampled grating periodicity of 10 μm. (b) The blue-shifted wavelengths as a function of sampled grating periodicity for different cladding materials, with the same waveguide width of 9 μm.

Figure 4 presents the effects of the main QCL's parameters on the blue-shifted wavelengths of the ASG structure. The results are obtained from formula (5). Figure 4(a) shows the blue-shifted wavelengths as a function of waveguide width for different cladding materials. As the waveguide width decreases, the blue-shifted wavelengths quickly increase, reaching hundreds of nanometers. The blue-shifted wavelengths as a function of sampled grating periodicity for different cladding materials are plotted in Fig. 4(b). We note that a decrease in the refractive index of the cladding material leads to an increase in the blue-shifted wavelengths. These calculations show that the waveguide width and the cladding material can be used as design parameter to control the output wavelength.

4. Experimental demonstration

The structure of the active region in the QCL is grown through solid-source molecular-beam epitaxy. An active layer with a 40-cycle periodicity of about 2.4 μm is sandwiched between an upper and lower InGaAs confinement layer of thickness 200 nm and 300 nm, respectively. The grating is fabricated on the upper confinement layer through the holographic exposure and optical photolithography. The upper and lower InP cladding layers are grown through metal-organic chemical vapor deposition (CVD). Specifically, the lower waveguide layer is a 5 μm low-doped InP layer grown on an n-InP substrate, and the upper waveguide layer comprises a 3 μm low-doped InP layer, a 0.2 μm gradually doped InP layer, and 0.6 μm high-doped InP contact layer. The ordinary sampled grating and ASG were fabricated on the same epitaxial wafer to ensure consistency with the base grating and to reduce process errors. Details of the fabrication process are described below. A selective etching liquid is used to remove the upper waveguide layer, and then a uniform base grating is manufactured through holographic exposure. The sampled grating is prepared through conventional optical lithography with an etching depth of 120–150 nm (Fig. 5).

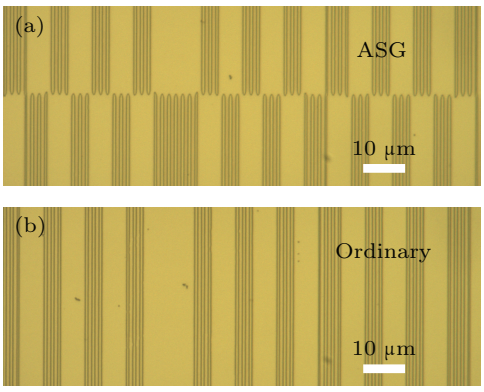


Fig. 5. Optical microscope images of (a) the ASG and (b) the ordinary sampled grating.

After the regrowth of the upper waveguide layer, a 450 nm thick SiO_2 mask is deposited with plasma-enhanced CVD, and the pattern is transferred through optical photolithography and wet etching to complete the fabrication of the double-channel waveguide. The average waveguide width is controlled to 9 μm, and then the Fe-doped InP is grown through metal-organic CVD to fill the double channels. After removing the SiO_2 mask by using hydrofluoric acid, another 450 nm thick SiO_2 layer is deposited as a passivation layer. After opening an

electric injection window on the ridge, the Ti/Au top contact electrode is evaporated by using an electron beam, and then the top contact electrode is thickened to 5 μm through electroplating to improve the heat dissipation performance. After being thinned and polished to 120 μm, a Ge/Au/Ni/Au layer is evaporated to form the bottom contact electrode. The epitaxial wafer is cleaved into a 3 mm long bar.

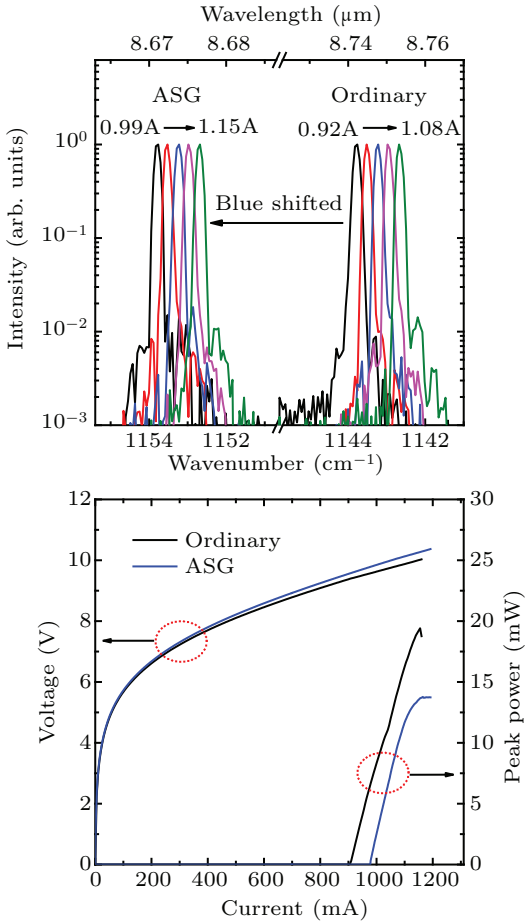


Fig. 6. (a) Emission spectra of the ordinary sampled grating and ASG QCLs under different injection currents. The wavelength of the ASG −1-th order mode is blue-shifted by 75.9 nm. The values of the current tuning coefficient for the ordinary sampled grating and ASG QCLs are $-6.8438\ \mathrm{cm^{-1}\cdot A^{-1}}$ and $-6.7813\ \mathrm{cm^{-1}\cdot A^{-1}}$, respectively. (b) Static characteristics of the two devices. The *P*–*I*–*V* characteristics of the ordinary sampled grating and ASG QCLs are marked in blue and black, respectively.

For an effective heat dissipation, the QCL is directly bonded epi-layer down to a copper submount with indium solder, then wire-bonded and mounted onto a holder containing a thermistor and a thermoelectric cooler to monitor and regulate the temperature, respectively. The emission spectrum is quickly scanned by using a Fourier transform infrared spectrometer with a resolution of 0.125 $\mathrm{cm^{-1}}$, and the optical power of the emission is measured by using a pyroelectric detector. All measurements were performed under continuous-wave operations at 20 °C. The emission spectra of the ordinary sampled grating and ASG QCLs under different injection currents are shown together to verify the effect of modulation on the wavelength of −1-th order mode of the ASG (Fig. 6(a)). Both QCLs show a single-mode operation over the entire dynamic range, and the emission spectrum is linearly proportional to the current, which proves that no mode-hopping occurs. By comparing the −1-th order mode at the threshold current (or the same current interval above the threshold) directly, the wavelength is seen to be blue-shifted by approximately 75.9 nm, which matches well the simulation results obtained here. If the red-shift in wavelength caused by current heating is also considered, the wavelength of the −1-th order mode then is blue-shifted to approximately 79.4 nm, which is slightly larger than the simulation results. The discrepancy is entirely attributed to modeling error.

The static power–current–voltage (*P*–*I*–*V*) characteristics (Fig. 6(b)) for the ASG QCL (blue line) and the ordinary sampled grating QCL (red line) show that the threshold current of the ASG QCL has increased and its peak power is reduced. The threshold current can be calculated by the following equation:[23]

$$J_{\mathrm{th}} = e\frac{\alpha_{\mathrm{tot}}/g_{\mathrm{c}} + n_2^{\mathrm{therm}}}{\tau_{\mathrm{eff}}}, \tag{6}$$

where e is elementary charge, τ_{eff} the effective lifetime, n_2^{therm} the material intrinsic parameters, α_{tot} the total modal loss (sum of the waveguide and mirror losses) and g_{c} the gain cross-section. Both devices are manufactured on the same epitaxial wafer and therefore have the same material parameters, except for g_{c} and α_{tot}. The gain cross-section g_{c} can be written as[23]

$$g_{\mathrm{c}} = \Gamma\frac{4\pi e^2}{\varepsilon_0 n_{\mathrm{reff}}\lambda}\frac{z_{32}^2}{2\gamma_{32}L_{\mathrm{p}}}, \tag{7}$$

where z_{32} is the dipole matrix element, $2\gamma_{32}$ is the FWHM broadening of the transition, n_{reff} the refractive index, λ the wavelength, and L_{p} the length of the period. Except for the optical confinement factor, all other parameters are related to the epitaxial material. We calculated the light confinement factors by integrating the square of the electric field (normE) of both gratings by using the FEM solver. The composition and dimensions of the simulation model are set to be the same as those of part III. The simulation results show that the optical confinement factor of the horizontal section of the ordinary sampled grating structure is about 92%, which is higher than that of the ASG structure (low 80%). At the same time, the reduction of the optical confinement factor leads to an increase in the total modal loss. Therefore, we believe that the reduction of the optical confinement leads to an increase in threshold current.

5. Conclusion

We have described the design and manufacture of an ASG structure based on QCL technology for selection of the mode.

The wavelength of the −1-th order mode is blue-shifted more than 75 nm ($\sim$ 10 cm^{-1}) with the emission wavelength of around 8.6 μm. Moreover, the current tuning coefficient is consistent with that of an ordinary sampled grating device. The structure of the ASG was fabricated in holographic exposure and optical photolithography because the base grating is uniform. Combined with the FEM simulation results, we demonstrated that this structure is insensitive to fluctuations in size of the two channels of the grating, assuming that the overall waveguide width remains constant. The output wavelength can be tailored freely within a certain range by adjusting the width of the ridge and the material of cladding layer, both of which improve the continuous tuning capability of the QCL array significantly.

Data availability

The data that support the findings of this study are available from the corresponding author upon reasonable request.

Acknowledgements

Project supported by the National Basic Research Program of China (Grant No. 2021YFB3201900), in part by the National Natural Science Foundation of China (Grant Nos. 61991430, 61774146, 61790583, 61627822, and 61774150), in part by the Key Projects of the Chinese Academy of Sciences (Grant Nos. 2018147, YJKYYQ20190002, QYZDJ-SSW-JSC027, and XDB43000000).

The authors thank Ping Liang and Ying Hu for their help in processing.

References

[1] Faist J, Capasso F, Sivco D L, Sirtori C, Hutchinson A L and Cho A Y 1994 *Science* **264** 553

[2] Gmachl C, Capasso F, Sivco D L and Cho A Y 2001 *Rep. Prog. Phys.* **64** 1533

[3] Zhao Y, Yan F L, Zhang J C, Liu F Q, Zhuo N, Wang L J and Wang Z G 2017 *J. Semicond.* **38** 074005

[4] Hou C C, Zhao Y, Zhang J C, Zhai S Q, Zhuo N, Liu J Q, Wang L J, Liu S M, Liu F Q and Wang Z G 2018 *J. Semicond.* **39** 034001

[5] Fei T, Zhai S Q, Zhang J C, Zhuo N, Liu J Q, Wang L J, Liu S M, Jia Z W, Li K, Sun Y Q, Guo K, Liu F Q and Wang Z G 2021 *J. Semicond.* **42** 112301

[6] Namjou K, Cai S, Whittaker E A, Faist J, Gmachl C, Capasso F, Sivco D L and Cho A Y 1998 *Opt. Lett.* **23** 219

[7] Fuchs F, Hugger S, Kinzer M, Aidam R, Bronner W, Lösch R, Yang Q K, Degreif K A and Schnurer F H 2010 *Opt. Engineer.* **49** 111127

[8] Curl R F, Capasso F, Gmachl C, Kosterev A A, McManus B, Lewicki R, Pusharsky M, Wysocki G and Tittel F K 2010 *Chem. Phys. Lett.* **487** 1

[9] Guo Q Q, Zhang J C, Ning C, Zhuo N, Zhai S Q, Liu J Q, Wang L J, Liu S M, Jia Z W and Liu F Q 2022 *ACS Photonics* **9** 1172

[10] Faist J, Gmachl C, Capasso F, Sirtori C, Sivco D L, Baillargeon J N and Cho A Y 1997 *Appl. Phys. Lett.* **70** 2670

[11] Rauter P and Capasso F 2015 *Laser Photo. Rev.* **9** 452

[12] Zhang J C, Liu F Q, Yao D Y, Zhuo N, Wang L J, Liu J Q and Wang Z G 2013 *J. Appl. Phys.* **113** 153101

[13] Zhuo N, Zhang J, Liu F, Wang L, Tan S, Yan F, Liu J and Wang Z 2013 *IEEE Photo. Tech. Lett.* **25** 1039

[14] Centeno R, Marchenko D, Mandon J, Cristescu S M, Wulterkens G and Harren F J M 2014 *Appl. Phys. Lett.* **105** 261907

[15] Liu C W, Zhang J C, Yan F L, Jia Z W, Zhao Z B, Zhuo N, Liu F Q and Wang Z G 2017 *Chin. Phys. Lett.* **34** 034209

[16] Slivken S, Bandyopadhyay N, Tsao S, Nida S, Bai Y, Lu Q Y and Razeghi M 2012 *Appl. Phys. Lett.* **100** 261112

[17] Mansuripur T S, Menzel S, Blanchard R, Diehl L, Pflügl C, Huang Y, Ryou J, Dupuis R D Loncar M and Capasso F 2012 *Opt. Exp.* **20** 23339

[18] Lee B G, Belkin M A, Pflugl C, Diehl L, Zhang H A, Audet R M, MacArthur J, Bour D, Corzine S, Hofler G and Capasso F 2009 *IEEE J. Quant. Electr.* **45** 554

[19] Jia X F, Wang L J, Zhuo N, Zhang J C, Zhai S Q, Liu J Q, Liu S M, Liu F Q and Wang Z 2018 *Photo. Res.* **6** 721

[20] Cheng F M, Jia Z W, Zhang J C, Zhuo N, Zhai S Q, Wang L J, Liu J Q, Liu S M, Liu F Q and Wang Z G 2017 *Photo. Res.* **5** 320

[21] Zhao Y, Zhang J C, Jia Z W, Liu Y H, Zhuo N, Zhai S Q, Liu F Q and Wang Z G 2016 *Chin. Phys. Lett.* **33** 124201

[22] Shi Y, Zhou Y, Li S, Guo R, Lu L, Feng Y and Chen X 2011 *IEEE Photo. Tech. Lett.* **23** 1337

[23] Faist J 2013 *Quant. Cascade Lasers* (Oxford Univ. Press) p. 114